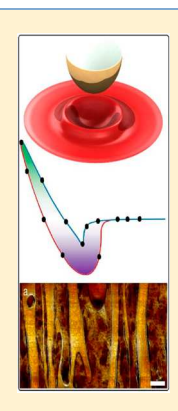
Dynamic AFM on Viscoelastic Polymer Samples with Surface Forces

Bahram Rajabifar, †,‡ Jyoti M. Jadhav, †,‡ Daniel Kiracofe, †,‡ Gregory F. Meyers,§ and Arvind Raman*,†,‡

Supporting Information

ABSTRACT: Dynamic atomic force microscopy (dAFM) is widely used to characterize polymer viscoelastic surfaces in the air/vacuum environments; however, the link between the instrument observables (such as energy dissipation or phase contrast) and the nanoscale physical properties of the polymer surfaces (such as local viscoelasticity, relaxation, and adhesion) remains poorly understood. To shed light on this topic, we present a computational method that enables the prediction and interpretation of dAFM observables on samples with arbitrary surface forces and linear viscoelastic constitutive properties with a first-principles approach. The approach both accelerates the computational method introduced by Attard and embeds it within the tapping mode amplitude reduction formula (or, equivalently, frequency modulation frequency shift/damping formula) to recover the force history and instrument observables as a function of the set point amplitude or Z distance. The method is validated against other reliable computational codes. The role of surface forces and polymer relaxation times on the phase lag, energy dissipation, and surface deformation history is clarified. Experimental data on energy dissipation in tapping mode/amplitude modulation AFM (TM-AFM/AM-AFM) for different free amplitudes and set point ratios are presented on a three-polymer blend consisting of well-dispersed phases of polypropylene, polycarbonate, and elastomer. An approach to experimental validation of the computational results is presented and analyzed.



1. INTRODUCTION

Downloaded via PURDUE UNIV on February 18, 2019 at 06:12:53 (UTC). See https://pubs.acs.org/sharingguidelines for options on how to legitimately share published articles.

Dynamic atomic force microscopy (dAFM) offers many advantages and unique capabilities for the nanoscale characterization of advanced polymeric materials. 1-6 dAFM enables the high-resolution imaging of polymer samples in air/vacuum/ liquid environments with gentle normal and lateral forces, thus allowing for minimally invasive imaging of these soft samples. Moreover, dAFM mode imaging always provides additional channels of observables (phase contrast, energy dissipation, higher harmonics, bimodal phase, etc.), which can be used to render nanoscale compositional contrast^{8,9} to complement topography images.

However, the dAFM compositional contrast on polymers can arise from different material properties (elasticity, viscoelasticity, relaxation times, hysteretic, van der Waals (vdW) adhesion, etc.) and depends on the operating conditions (set point ratio, free amplitude, drive frequency, stiffness, tip radius, and quality factor). Because of the variety of effective parameters that characterize the physical properties of polymers, the interpretation of the instrument's observables on polymer samples is difficult.

To understand the link between dAFM compositional contrast on polymers and local material properties, a mathematical model that predicts the interaction between the dAFM oscillating tip and the viscoelastic sample surface is required. For example, to interpret contact-mode related AFM methods such as force modulation or contact resonance, viscoelastic sample models without surface forces are often used. 11-17 However, such approaches cannot be applied to dAFM, where the tip intermittently interacts with the viscoelastic sample surface and requires an accurate and selfconsistent inclusion of both surface forces and surface relaxation dynamics.

Prior efforts linking dAFM compositional contrast on polymers to local properties have key limitations. Early works suggested that dAFM phase contrast under moderate tapping conditions on polyethylene was merely correlated to polymer density and elasticity rather than viscoelastic properties. More commonly, in mathematical simulations of dAFM, viscoelasticity is introduced as an ad hoc addition of a Kelvin-Voigt viscoelasticity model within Hertzian or DMT (Derjaguin, Muller, and Toporov) contact mechanics theories. 11-17

$$F_{ts}(d, \dot{d}) = \begin{cases} 0, & d > 0 \\ \frac{4}{3} E^* \sqrt{R} (-d)^{3/2} - \eta \dot{d} \sqrt{-Rd}, & d \le 0 \end{cases}$$
(1)

where the tip-sample interaction force F_{ts} depends on the tipsample gap *d* and tip velocity *d* through the effective tip—sample elastic modulus E^* , sample viscosity η , and tip radius R. There are two fundamental problems with this ad hoc model. First, when the oscillating tip is interacting with the sample (d < 0) and

Received: September 10, 2018 Revised: October 28, 2018 Published: November 21, 2018

[†]School of Mechanical Engineering, Purdue University, 585 Purdue Mall, West Lafayette, Indiana 47907, United States

[‡]Birck Nanotechnology Center, 1205 W. State Street, West Lafayette, Indiana 47907, United States

[§]Analytical Sciences, The Dow Chemical Company, 1897 Building, Midland, Michigan 48667, United States

it is withdrawing from the sample (d>0), it is possible that $F_{\rm ts}<0$ for sufficiently large d and η . However, the Hertz contact model should only include repulsive surface forces $(F_{\rm ts}\geq0)$, so this outcome of the model (eq 1) is nonphysical. Put another way, as the tip withdraws, the deformed sample does not return to its original condition instantly, but rather it takes time to relax due to viscoelasticity, allowing the tip to detach from the sample before d=0. However, the $ad\ hoc$ model cannot account for this and applies an attractive force forcing the tip to withdraw only as fast as the sample can relax. This is seen clearly in a force—indentation history during a single tap that is simulated using Hertz contact mechanics with an $ad\ hoc$ Kelvin—Voigt viscoelasticity model which is generated by VEDA (virtual environment for dynamic AFM), ¹⁸ as shown in Figure 1. The

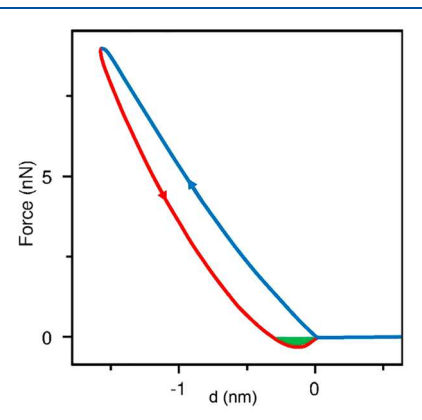


Figure 1. F-d history during a single tapping cycle predicted by the AMAC tool in VEDA²⁸ using the Hertz model including Kelvin–Voigt viscoelasticity in an *ad hoc* manner. The computation uses these parameters: free amplitude: 60 nm; natural and driving frequency: 75 kHz; Q = 150; approach velocity: 200 nm/s; tip radius: 10 nm. The viscoelastic properties used are E = 1 GPa and $\eta = 100$ Pa·s. Note that the retraction phase features a region of attractive forces shaded in green which is an artifact of the underlying model assumptions.

presence of attractive forces during the retraction phase arises from the ad hoc and incorrect assumption that the contact area history of the tip during the retraction phase of the oscillation for a viscoelastic material is not different from that of a purely elastic material. In contrast, Ting's model¹⁹ modifies the Hertzian contact model by using the viscoelastic correspondence principle and correctly predicts the contact area evolution for tip interaction with a linear viscoelastic solid. However, since surface forces are ignored in Ting's model, it cannot predict surface deformations occurring before tip-sample contact or spontaneous and nonequilibrium surface instabilities such as sample snap off and jump to contact with the tip. These phenomena are especially relevant for dAFM on soft materials or viscoelastic surfaces with a moderate to large adhesion. In recognition of the likely role of surface relaxation in dAFM, recent works^{20,21} have included surface relaxation within dAFM simulations and modeled the contact as a bed of linear springs and viscous dashpots. However, they do not consider contact mechanics, 3D continuum viscoelasticity, and surface forces in a self-consistent manner.

In summary, understanding dAFM on polymers needs computational approaches in which the relevant physics of the interactions are taken into account in a self-consistent manner. Attard and co-workers^{22–26} introduced a completely different approach for including the relevant physics of the contact

between a tip and an adhesive viscoelastic surface within the Boussinesq solution²⁷ of a tip—sample contact problem. The approach is akin to a boundary element method in that the sample surface is discretized with a mesh and the surface deformation and pressure are computed at each mesh point in time explicitly. Attard's approach does away with *ad hoc* assumptions of prior models discussed before and computes the surface deformation field self-consistently using 3D linear elasticity/viscoelasticity and arbitrary surface forces. However, since the algorithm is based on an iterative loop, it is computationally expensive. Moreover, the approach requires precise knowledge of the tip motion, which is not known *a priori* in dAFM, but rather depends on the material properties and operating conditions.

In this work, we both accelerate the computational method introduced by Attard and embed it within the tapping mode amplitude reduction formula (or, equivalently, frequency modulation frequency shift/damping formula) to recover the instrument observables (phase contrast/energy dissipation) and force and surface deformation history as a function of the set point amplitude or Z distance over adhesive viscoelastic surfaces. The algorithm allows for the self-consistent inclusion of resonant microcantilever dynamics, surface forces, and linear three-dimensional material viscoelasticity within dAFM simulations. The approach is validated by comparison with the results of Attard²² as well as with VEDA simulations using Ting's model. 19 The approach is then used to study the effects of polymer relaxation modes and surface forces on interaction force and surface deformation history and TM-AFM/AM-AFM observables such as energy dissipation and phase. Experimental data acquired using TM-AFM/AM-AFM on energy dissipation on a blend of polypropylene, polycarbonate, and elastomer are described. An approach to for the experimental validation of computational results is presented and analyzed.

2. RESULTS AND DISCUSSION

2.1. Theory of the Proposed Approach. In AM-AFM (commonly known as TM-AFM), a microcantilever with a sharp tip is excited near its fundamental frequency, and the microcantilever's vibration while interacting with the surface of the sample is monitored via a beam bounce technique. Here we review some key concepts from the analytical theory of AM-AFM upon which the proposed approach is based, recognizing that the proposed approach can be easily adapted for frequency modulation AFM (FM-AFM).

For steady-state AM-AFM oscillations in air/vacuum, the tip settles in a well-defined motion,²⁹ which is dominated by the fundamental harmonic of tip motion: $q(t) = A \sin(\omega t - \phi)$, where q(t) is the tip deflection, A is the amplitude of the oscillation, and ϕ is the phase lag relative to the excitation force. Higher harmonics also occur, but they are about 2 orders of magnitude smaller than the fundamental in air or vacuum applications.^{30,31} If we assume that the higher harmonics of tip displacement are negligible compared to the primary harmonic, the unperturbed distance of the tip above the sample surface is Z, which is adjusted by the Z piezo, the tip-sample gap is d(t) = Z+ q(t), and d is the tip velocity. A schematic of an oscillating tip interacting with a sample is illustrated in Figure 2. During the interaction time, the tip experiences local surface forces, both conservative and nonconservative. The oscillation amplitude A of the resonant probe decreases once the Z piezo approaches, and the microcantilever begins to interact with the sample

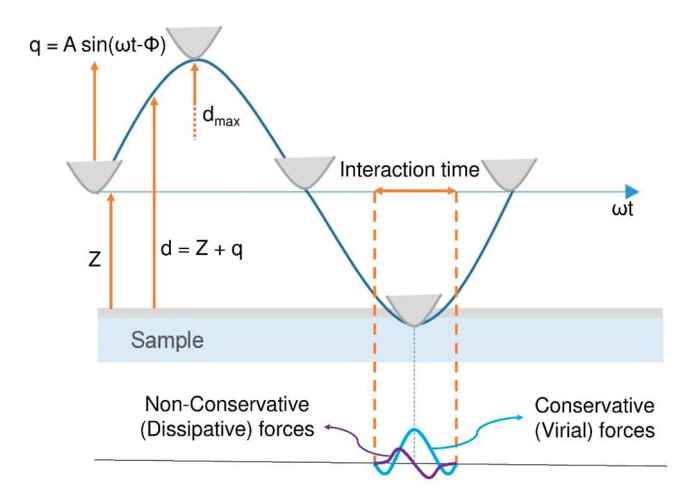


Figure 2. Schematic of an oscillating tip with tip—sample dissipative and conservative forces. d (nm) is the tip—sample gap, and Z (nm) is the distance between the unperturbed microcantilever tip and the sample. The average of interaction force history during approach and retraction is the conservative part of interaction since it depends on the instantaneous tip—sample gap d and contributes to the virial, while the difference of the approach and retraction force history during a cycle is the nonconservative part of the interaction and contributes to the energy dissipation.

surface. Under these conditions, the virial $V_{ts}(A,Z)$ and energy dissipation $E_{ts}(A,Z)$ can be calculated as follows:

$$V_{ts} = \frac{1}{T} \int_{0}^{T} F_{ts}(Z + A \sin(\omega t - \phi),$$

$$\dot{Z} + A\omega \cos(\omega t - \phi))A \sin(\omega t - \phi) dt = V_{ts}(A, Z)$$

$$(2)$$

$$E_{ts} = \int_{0}^{T} F_{ts}(Z + A \sin(\omega t - \phi),$$

$$\dot{Z} + A\omega \cos(\omega t - \phi))A\omega \cos(\omega t - \phi) dt = E_{ts}(A, Z)$$

$$(3)$$

where $F_{\rm ts}$ is the tip—sample interaction force and T is the time period of the oscillation. Furthermore, $A^{\rm ratio} = A/A^{\rm free}$, known as the amplitude set point ratio (dimensionless), is the ratio of the resonant amplitude A during interaction and the free amplitude $(A^{\rm free})$ far from the sample. $A^{\rm ratio}$ is related to $E_{\rm ts}(A,Z)$ and $V_{\rm ts}(A,Z)$ using the amplitude reduction formula, which is derived by rearranging the virial and energy dissipation equations $^{32-34}$ of AM-AFM. Specifically

$$A^{\text{ratio}} = \frac{1/Q}{\sqrt{\left(\frac{-2V_{\text{ts}}(A,Z)}{kA^2}\right)^2 + \left(\frac{1}{Q} + \frac{E_{\text{ts}}(A,Z)}{\pi kA^2}\right)^2}}$$
(4)

where $V_{\rm ts}$ (eV/cycle) is the virial, $E_{\rm ts}$ (eV/cycle) is the energy dissipation, k (N/m) is the equivalent microcantilever stiffness of the driven eigenmode,³⁵ and Q is the quality factor of the microcantilever. Equation 4 highlights the implicit relationship between amplitude reduction and tip—sample interactions. In particular, the amplitude A appears both on the left-hand side and on the right-hand side (through the $E_{\rm ts}$ and $V_{\rm ts}$ terms) of eq 4.

We propose an algorithm for using eq 4 to find the Z-distance for each desired/observed A^{ratio} and thus predict the AM-AFM observables and surface deformation and force history as a function of *A*^{ratio}. As illustrated in Figure 3, *A*^{ratio}_{current} is the desired/ observed amplitude ratio, $A_{\text{new}}^{\text{ratio}}$ is the computed amplitude ratio, tol is the tolerance band, dZ (nm) is a small decrement in Z, and ΔZ is the initial guess for the Z piezo increment. The value for dZ is updated at each iteration to facilitate a faster convergence. In the proposed approach, the procedure starts with an initially guessed Z-distance value, which is adjusted (increased/ decreased) such that the A^{ratio} obtained by computing E_{ts} and $V_{\rm ts}$ using Attard's method and inserting into the right-hand side of eq 3 matches the desired $A^{\rm ratio}$ on the left-hand side of eq 3, within tol, the defined tolerance. When the difference between the computed and desired A^{ratio} falls within tol, all observables like Z, energy dissipation, virial, indentation, amplitude, tipsample force history, sample deformation history are recorded for the specific A^{ratio} . Additionally, the phase lag ϕ can be calculated for each desired A^{ratio} as follows:

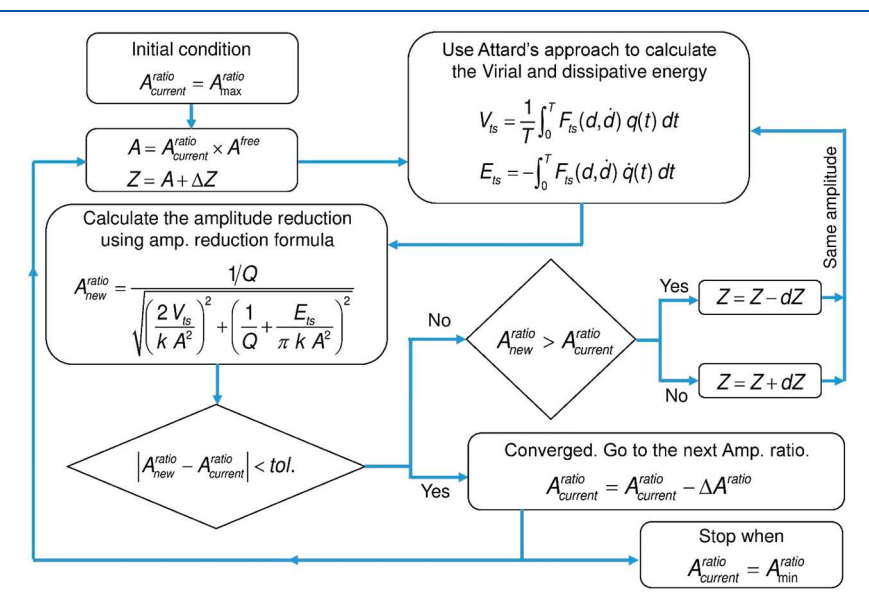


Figure 3. Proposed algorithm for predicting instrument observables by embedding Attard's model into the AM-AFM amplitude reduction formula.

$$\tan \phi = \frac{\frac{1}{Q} + \frac{E_{ts}(A, Z)}{\pi k A^2}}{\frac{-2V_{ts}(A, Z)}{k A^2}}$$
(5)

After meeting the tolerance criteria for a given $A^{\rm ratio}$, the algorithm goes to the next $A^{\rm ratio}$ in the range. The $A^{\rm ratio}$ range considered in the flowchart (Figure 3) is between and $A^{\rm ratio}_{\rm min}$ with $\Delta A^{\rm ratio}$ steps. The advantage of the above algorithm is that it allows for the computation of the amplitude/phase/energy dissipation as a function of $A^{\rm ratio}$ without time-domain simulations of nonlinear governing equations of AFM microcantilever dynamics as in VEDA.

The described algorithm (Figure 3) thus only needs the fast computation of $E_{\rm ts}$ and $V_{\rm ts}$ using Attard's model^{22–26} for tip oscillation amplitudes A and Z distances for which it is called to execute. The underlying principle of Attard's model is highlighted in Figure 4, where an axisymmetric rigid tip is

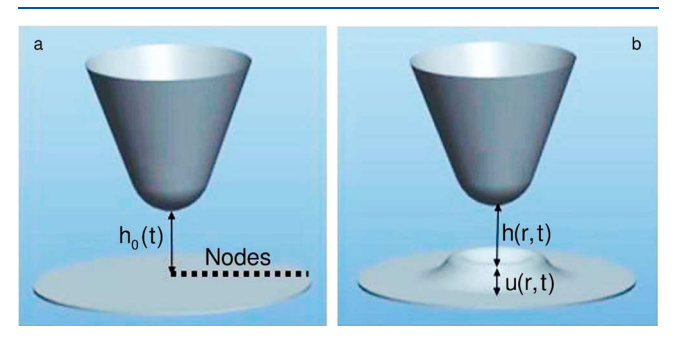


Figure 4. Attard's viscoelastic model assumes an axisymmetric rigid tip interacting with a flat polymer surface. To model the viscoelasticity of the sample, creep compliance of a standard three-element viscoelastic model is utilized eq 8³⁶ in conjunction with arbitrary surface force models. (a) and (b) show the undeformed and deformed sample, respectively.

shown in close proximity to the sample surface. The radial coordinate r measures the radial distance along the undeformed surface from the projected location of the center of the tip. $h_0(r,t)$ is the gap between the tip and the undeformed surface. Specifically, when called by the proposed algorithm (Figure 3), with a specific A, Z, and ω value, $h_0(r,t)$ takes the following explicit time-dependent form:

$$h_0(r, t) = (Z + A \sin(\omega t)) + \frac{r^2}{2R}$$
 (6)

Furthermore, u(r,t) is the vertical displacement (deformation) of the sample, $h(r,t) = h_0(r,t) - u(r,t)$ is the gap profile between the tip and the deformed surface, and the illustrated nodes (Figure 4) show the spatial discretization on the surface of the sample. The spatial discretization is referred to by i/j indices. The Lennard-Jones pressure accounts for the surface force between the tip and the sample:

$$p(h(r,t)) = \frac{H}{6\pi h(r,t)^3} \left(\frac{z_0^6}{h(r,t)^6} - 1 \right)$$

$$= \frac{H}{6\pi (h_0(r,t) - u(r,t))^3} \left(\frac{z_0^6}{(h_0(r,t) - u(r,t))^6} - 1 \right)$$
(7)

where H is the Hamaker constant and z_0 is the equilibrium distance. Alternative surface force models can also be included in

the approach. The viscoelasticity of the sample is incorporated by the creep compliance of a standard linear solid (three element) viscoelastic model;³⁶ however, the approach can in principle include any linear viscoelastic constitutive relation:

$$\frac{1}{E(t)} = \frac{1}{E_{\infty}} + \frac{E_{\infty} - E_0}{E_{\infty} E_0} e^{-t/\tau}$$
(8)

$$\frac{1}{E(t)} = \frac{1 - \nu^2}{E_{\rm s}(t)} \tag{9}$$

where $E_{\rm s}(t)$ and E(t) are the time-dependent Young modulus and reduced elastic modulus of the sample as defined in eq 9, respectively, E_0 and E_∞ are short- and long-time reduced Young's modulus of the sample $(E_0 > E_\infty)$, and τ is the relaxation time for the creep compliance function. The rate of the change of the sample surface deformation and its deformation is correlated by 23

$$\dot{u}(r,t) = -\frac{1}{\tau} (u(r,t) - u_{\infty}(r,t))$$

$$-\frac{1}{E_0} \int_0^\infty k(r,s) \dot{p}(h(s,t)) s \, ds$$
(10)

where \dot{u} and \dot{p} are time derivatives of sample deformation and the pressure, respectively. The long time static deformation (u_{∞}) and k(r,s) are given by

$$u_{\infty}(r, t) = -\frac{1}{E_{\infty}} \int_0^{\infty} k(r, s) p(h(s, t)) s \, \mathrm{d}s$$
(11)

$$k(r,s) = \begin{cases} \frac{4}{\pi r} K(s^2/r^2) & s < r \\ \frac{4}{\pi s} K(r^2/s^2) & s > r \end{cases}$$
(12)

where K is the complete elliptical integral of the first kind. Equations 10 and 11 can be spatially discretized by trapezoidal integration as follows:

$$\dot{u}(r_i, t) = -\frac{1}{E_0} \sum_{j=1}^{N} \dot{p}(h(r_j, t)) \Delta r_j k(r_i, r_j) r_j$$

$$-\frac{1}{\tau} (u(r_i, t) - u_{\infty}(r_i, t))$$
(13)

$$u_{\infty}(r_i, t) = -\frac{1}{E_{\infty}} \sum_{j=1}^{N} p(h(r_j, t)) \Delta r_j k(r_i, r_j) r_j$$
(14)

where $\Delta r_j = r_j - r_{j-1}$ and N is the number of radial nodes. As can be seen, \dot{u} appears explicitly and implicitly (through $\dot{p}(h)$) on both sides of eq 13. To solve this equation, Attard^{23,24} used a slow iterative approach in which a value of \dot{u} is guessed at each time step and refined iteratively until the left and right-hand sides of eq 13 are within a defined tolerance.

It is important to emphasize that Attard's model represents the exact solution to the field equations of 3D elasticity and through the correspondence principle allows for any linear viscoelastic constitutive relationship to be included. Interested readers are referred to Attard's papers for a complete theory of the employed model.^{22–25}

In contrast to Attard's algorithm for solving these equations, we propose to take all the explicit \dot{u} terms in eq 13 to the left side as follows:

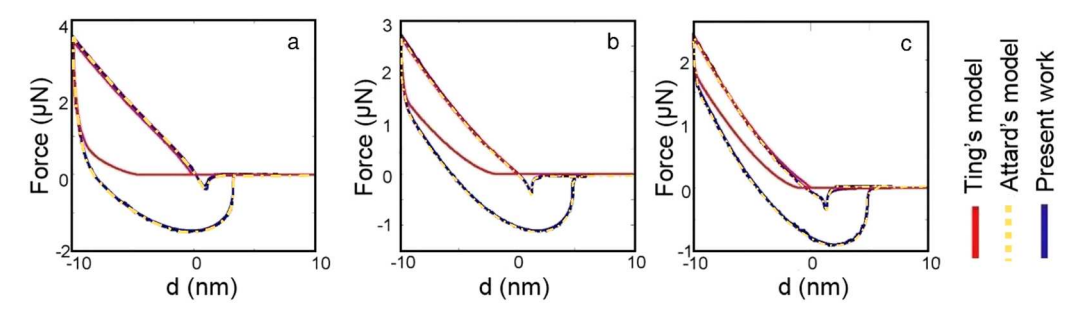


Figure 5. Attard's viscoelastic model results, ²² Ting's analytical viscoelastic model²⁸ and the code developed in the present work are compared with a prescribed triangular motion time profile of a rigid spherical tip. The triangular drive velocities are (a) $\pm 5 \,\mu$ m/s, (b) $\pm 2 \,\mu$ m/s, and (c) $\pm 1 \,\mu$ m/s. The tip radius is 10 $\,\mu$ m, and the other material parameters used are identical to the ones used by Attard to facilitate comparison. ²²

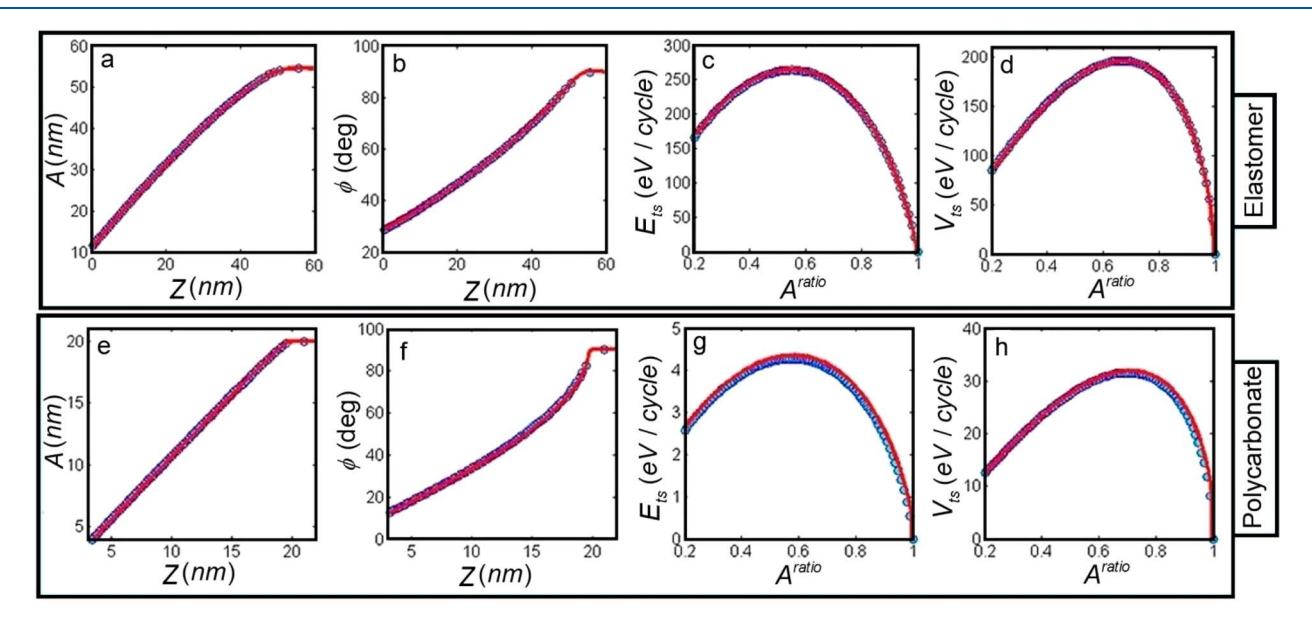


Figure 6. A comparison between the dynamic approach curves results predicted by using the present algorithm (**Figure 3**) and the ones from the AMAC tool which includes explicit microcantilever dynamics for elastomer (upper row) and polycarbonate (lower row). The blue circles are from the proposed algorithm, and the red solid lines are the VEDA-AMAC tool's outputs. The used material property data for these simulations are listed in **Table 1**. The equivalent microcantilever properties are K = 28 N/m and Q = 542, and the oscillation period is 3×10^{-6} s.

$$\dot{u}(r_i, t) = J_{ij}^{-1} b_i \tag{15}$$

$$J_{ij} = \frac{1}{E_0} (p'(h(r_j, t)) \Delta r_j k(r_i, r_j)) - \delta_{ij}$$
(16)

$$b_i = \frac{1}{E_0} \sum_{j=1}^{N} p'(h(r_j, t)) \dot{h}_0(r_j, t) \Delta r_j k(r_i, r_j) r_j$$

$$+ \frac{1}{\tau} (u(r_i, t) - u_{\infty}(r_i, t))$$
 (17)

$$p'(h(r_j, t)) = \frac{\mathrm{d}p}{\mathrm{d}h} = \frac{H}{2\pi(h_0(r_j, t) - u(r_j, t))^4}$$

$$\times \left(1 - \frac{3z_0^6}{(h_0(r_j, t) - u(r_j, t))^6}\right) \tag{18}$$

where δ_{ij} is the Kronecker delta. Equation 15 is thus a large set of nonlinear coupled ordinary differential equations with explicit time-dependent forcing through the $h_0(r_{ij}t)$ term. This is solved by discretizing time and evaluating the left-hand side of eq 14 at each time step and using the deformation velocities at the nodes to step forward to the new position of the deformed surface. The

code is implemented in both FORTRAN for future deployment in VEDA and in MATLAB. In both codes, the time is discretized per uniform increments/decrements of the tip—sample gap (d), and the surface is spatially discretized into nodes with equal radial increments. The selection of the appropriate number of temporal/radial discretization points is made through numerical studies to ensure that the solution is converged, and the predictions are independent of the number of discretization points. This allows for the explicit computation of $u(r_pt)$ and consequently $h(r_pt)$ and thus $p(h(r_pt))$. With this computation in place, it is easy to determine the tip—sample interaction force history as follows:

$$F_{ts}(t_k) = 2\pi \Delta r \sum_{j=1}^{N} p(h(r_j, t_k)) r_j$$
(19)

Once the tip—sample force history is calculated during an oscillation cycle for a specific Z and A value, the result can be plugged into eqs 3 and 4 to compute $E_{\rm ts}(Z,A)$ and $V_{\rm ts}(Z,A)$, which are needed to determine the Z value required to achieve a certain A and ϕ . Once this is computed as described in Figure 3, all the relevant dAFM observables such as sample deformation/

	τ (s)	E_0 (GPa)	E_{∞} (GPa)	Н (Ј)	z_0 (nm)	A_0 (nm)
elastomer	5.47×10^{-8}	0.143	0.029	7.99×10^{-20}	0.6	60
polycarbonate	6.56×10^{-8}	2.960	2.08	8.82×10^{-20}	0.3	20

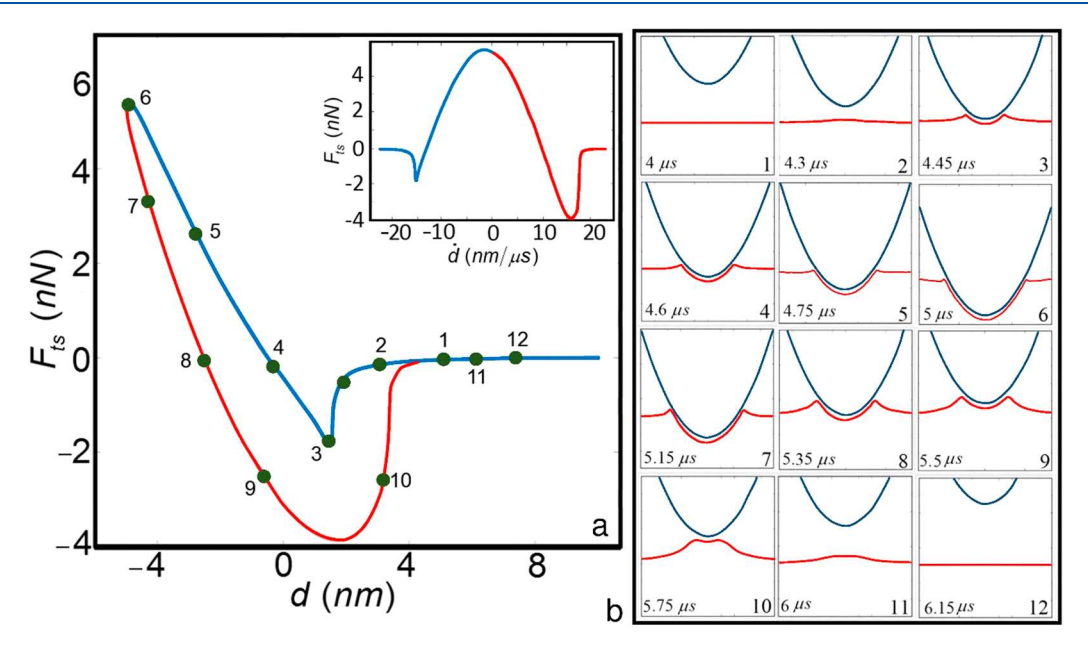


Figure 7. Interaction between a rigid axisymmetric tip and the elastomer sample surface is computed using the approach of the present work. The viscoelasticity of the elastomer is modeled by using a standard linear solid (SLS) model with the data provided in Table 1. The tip travels through a sinusoidal wave with $100 \, \text{kHz}$ frequency and $Z = 45 \, \text{nm}$. The oscillation amplitude is $50 \, \text{nm}$ and tip radius = $100 \, \text{nm}$. In (a) the F - d and the F - d history (inset) are graphed. In (b), the deformation history during a sequence of time instants labeled 1 - 12 is graphed. The full video is provided as the Supporting Information.

relaxation history per cycle, energy dissipation, force history, virial, phase lag, and so on can be determined at the desired A^{ratio} .

2.2. Verification. By directly solving the set of ODE's in the time domain rather than an iterative solver as in Attard's original work, the present approach is nearly an order of magnitude faster than the original computational approach presented by Attard. We present here the computational verification and validation of the proposed approach.

To verify the accelerated computational approach presented, we compare the predicted F-d histories for a prescribed triangular tip motion with the ones in Attard's original work (Figure 5).²² These results are also compared with simulations performed using identical parameters but using Ting's viscoelastic model of contact mechanics without surface forces, which is calculated by using the VEDA set of tools.²⁸ The number of temporal discretization points is 10⁴, the simulations are performed for an effective tip radius of 10 μ m, and 600 radial nodes are used within a radius of 500 nm of the surface to ensure convergence of the solution. The characteristic relaxation time for the creep function is 1 ms, the short-time Young's modulus of the sample (E_0) is 10 GPa, and the long-time Young's modulus of the sample (E_{∞}) is 1 GPa. For Attard's viscoelastic model, the Hamaker constant *H* is 10^{-19} J and the equilibrium position z_0 is 0.5 nm. A triangular oscillation with amplitude 20 nm with three different tip velocities is prescribed into the model, and h_0 oscillates between 10 and -10 nm. The predictions of the developed code predict excellently the ones presented by Attard²² and are in close agreement with Ting's model prediction during the approach phase but not during the

retraction phase. This result is consistent with the lack of surface forces in Ting's model.

Next, we validated the proposed algorithm (Figure 6) for computing the dynamic approach curves when using Attard's model for tip-sample interactions. AMAC (Amplitude Modulated Approach Curves) is an already validated tool on VEDA, which includes full microcantilever dynamics and makes reliable predictions for tapping mode AFM.²⁸ This tool can accurately use Ting's model (but not Attard's) as the tip-sample interaction model, which we choose for the validation of this algorithm. Therefore, the comparison between the instrument observables predicted by computing force-distance histories and embedding them within the AM-AFM amplitude reduction formula (Figure 3) and the ones computed directly from the AMAC tool help us to ensure the validity of the proposed algorithm. As illustrated in Figure 6, the A, ϕ , $V_{\rm ts}$, and $E_{\rm ts}$ graphs show an excellent match for both elastomer and polycarbonate material properties. Because polycarbonate is stiffer than the elastomer, the energy dissipation and virial values for the elastomer are greater than the ones of polycarbonate. The parameter values used for the polymers in these simulations are listed in Table 1.

2.3. Computational Results. To visualize the physics of the tip—sample interaction during a single cycle, a simulation is performed for a prescribed sinusoidal tip motion interacting with an elastomer sample (Figure 7). The elastomer sample is represented by a standard linear viscoelastic solid (three element) model with the data provided in Table 1. The complete set of parameters used for this simulation is provided in the caption of the figure. The number of temporal

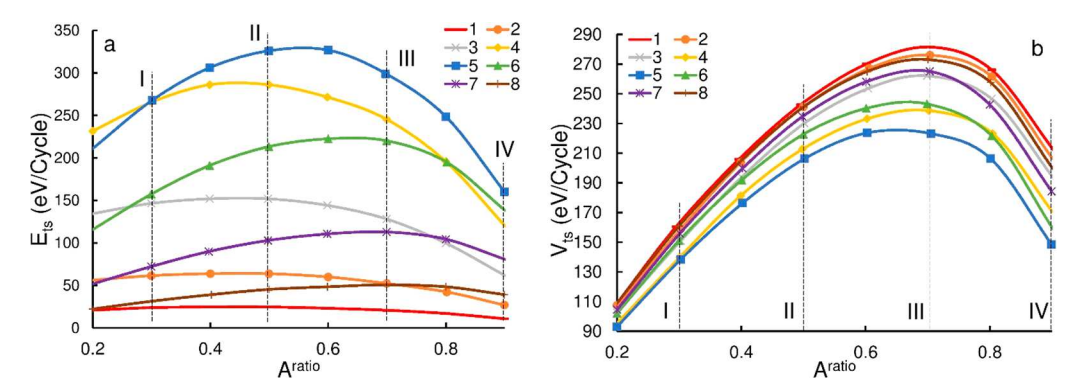


Figure 8. (a) Energy dissipation (E_{ts}) and (b) virial (V_{ts}) vs set point ratio (A^{ratio}) for a set of relaxation time (τ) values: 1:2.9 μ s, 2:1.1 μ s, 3:0.40 μ s, 4:0.15 μ s, 5:54.7 ns, 6:20.3 ns, 7:7.6 ns, and 8:2.8 ns. The Lennard-Jones parameters for all simulations are $H = 8 \times 10^{-20}$ J, and $Z_0 = 0.6$ nm; additional material properties are provided in Table 1 for the elastomer. The oscillation period is 3×10^6 s, the equivalent microcantilever properties are K = 28 N/m and Q = 542, and the tip radius is 15 nm. The vertical lines marked by Roman numerals are discussed in Figure 10.

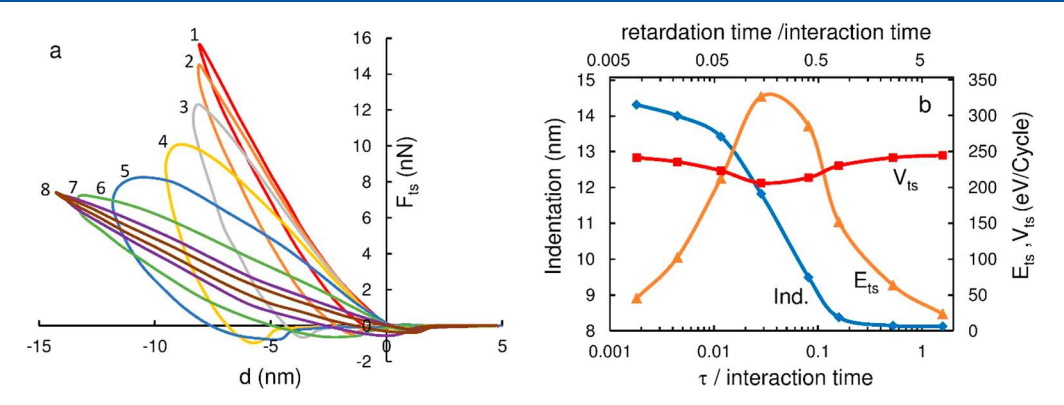


Figure 9. F-d histories and indentation depth predictions at $A^{\rm ratio}=0.5$ for a range of relaxation times (τ) are demonstrated. The τ values and other simulation parameters are identical to the ones in Figure 8b. The indentation depth, $E_{\rm ts}$ and $V_{\rm ts}$ corresponding to the F-d histories in (a) are graphed as a function of τ nondimensionalized by the tip–sample interaction time. Note that each of the cycles 1-8 in (a) has a different interaction time.

discretization points is 105, the simulations are performed for an effective tip radius of 100 nm, and 100 radial nodes are used inside a radius of 50 nm on the surface to ensure convergence of the solution. Figure 7 shows the force history during one cycle as a function of d and \dot{d} (inset). These force histories clearly show the dependence of hysteresis and adhesion on both d and d. The series of tip-sample geometries corresponding to 12 instants during the force history (Figure 7b) is captured from the output video of the code, which is provided as the Supporting Information. During the tip approach, the material's surface slightly deforms upward from its initial flat state, then snaps on to the tip, and then deforms downward with the tip movement. However, it gradually peels away from the tip during the retraction process, until a final detachment occurs. After the detachment, the surface continues to relax until it returns to the initial state. These surface instabilities are in line with predictions by Attard's model.^{37,38} The cycle then repeats at every tap, unless the sample has not fully relaxed prior to a subsequent tap. This latter condition has not been explored in the present work where we assume the sample eventually fully relaxes prior to a subsequent tap. It is worth mentioning that the phenomena that are captured by the model and demonstrated in this figure are not fully accounted for by any of the classical models such as Hertz, JKR (Johnson, Kendall, and Roberts), DMT, or Ting's model.

To study the effect of diverse relaxation modes of polymers³⁶ on AM-AFM observables, a set of the relaxation times τ ranging between 2.9×10^{-6} and 2.8×10^{-9} s is used in the developed

code as prescribed in Figure 3, and their effect on the outputs of the model such as $V_{\rm ts}$, $E_{\rm ts}$, $F_{\rm ts}$, and indentation depth vs $A^{\rm ratio}$ is investigated. The relaxation time τ determines how fast the instantaneous Young's modulus of the sample changes from E_0 to E_{∞} . All the other parameters except τ are identical for all the simulations.

As illustrated in Figure 8, energy dissipation values are significantly affected by τ . $E_{\rm ts}$ reaches its maximal values at specific relaxation times. Figure 8a also demonstrates an additional key result. The $A^{\rm ratio}$ at which maximum energy dissipation occurs³⁹ is highly dependent on τ . However, as depicted in Figure 8b, contrarily, the $V_{\rm ts}$ does not vary substantially when τ is changed.

It is instructive to examine in Figure 9a the F-d histories acquired as a part of the simulations presented in Figure 8 for a fixed as the τ is changed in the stated range above. In Figure 9a, the force loops show minimal hysteresis when τ is small compared with the contact time and reach a maximum hysteresis when for an intermediate value of τ , and the hysteresis vanishes when τ is very large. To be more quantitative, we estimate the contact (interaction) time in each F-d history in Figure 9a from the time $A^{\rm ratio}=0.5$ spent in the repulsive interaction regime. Then we plot the corresponding indentation, $E_{\rm ts}$ and $V_{\rm ts}$ as a function of τ nondimensionalized by the contact time in Figure 9b, all at $A^{\rm ratio}=0.5$. Figure 9b illustrates that the indentation depth increases with decreasing τ . For $\tau \ll$ contact time, the material has enough time to completely relax during the interaction time, and therefore the modulus behaves more like

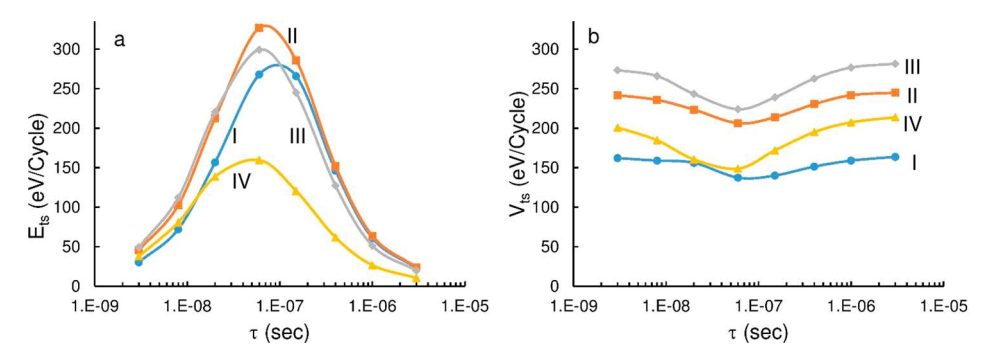


Figure 10. (a) Energy dissipation (E_{ts}) vs relaxation time (τ) and (b) virial (V_{ts}) vs τ for a series of $A^{ratio} = 0.3$, 0.5, 0.7, and 0.9 that are specified in Figure 8 by vertical dashed lines labeled I, II, III, and IV, respectively. All of the simulation parameters are identical to the ones in Figure 8.

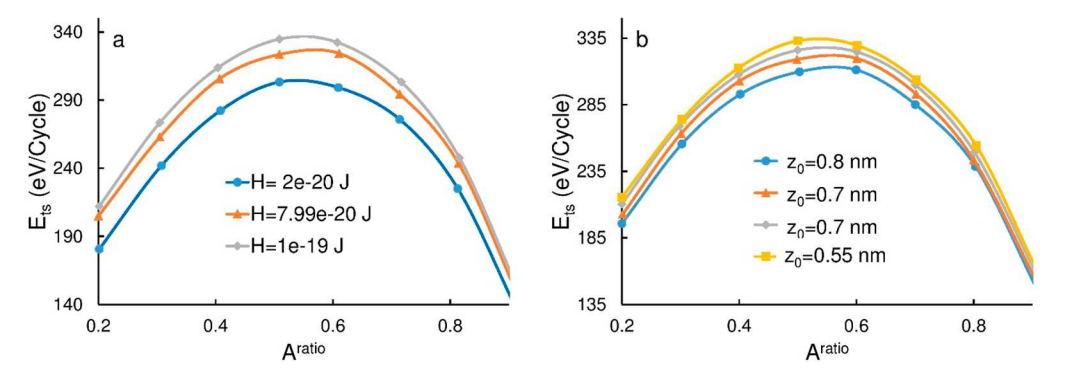


Figure 11. Energy dissipation (E_{ts}) vs set point ratio (A^{ratio}) for (a) different Hamaker (H) constant values and (b) different values of equilibrium position (z_0). For (a) $z_0 = 0.6$ nm, and for (b) $H = 8 \times 10^{-20}$ J. The material properties are the ones recorded in Table 1 for the elastomer.

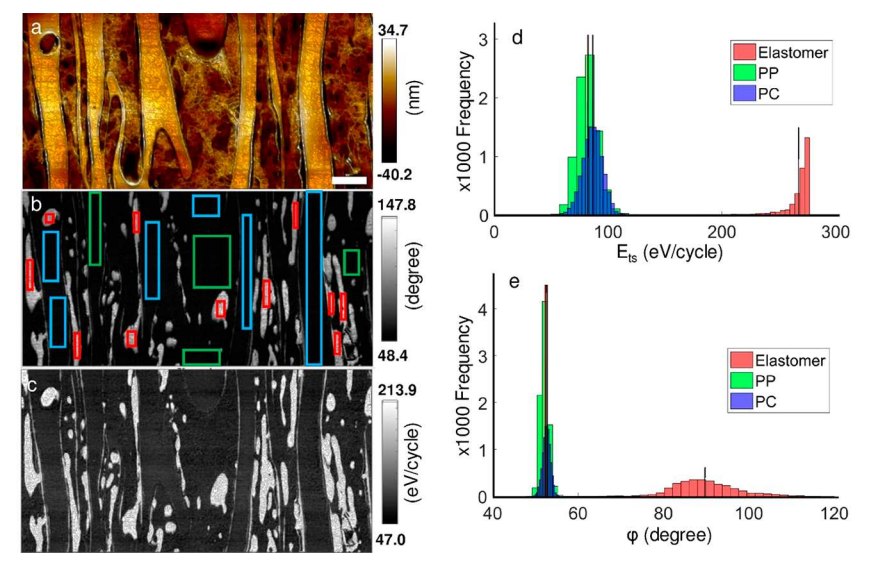


Figure 12. (a) Topography image, (b) phase lag image, and (c) extracted energy dissipation on a three-phase blend polymer sample with $A^{\text{ratio}} = 0.7$ and $A^{\text{free}} = 35.9$ nm. (d) and (e) show histograms of the extracted energy dissipation and phase lag values acquired over the selected rectangular areas of the PC, PP, and elastomer marked in (b) with corresponding colors. The vertical bold lines shown for each histogram in (d) and (e) represent the mean value for each polymer. The scale bar is shown in (a) represents 1 μ m.

 E_{∞} during both approach and retraction leading to a larger indentation and small hysteresis leading to low-energy dissipation $E_{\rm ts}$. Likewise, when $\tau\gg$ contact time, the material responds with a stiff E_0 leading to a less indentation and small hysteresis leading to low-energy dissipation $E_{\rm ts}$. Figure 9b shows that $E_{\rm ts}$ is maximized when $\tau/$ contact time $\sim 0.01-0.1$. Put another way, $E_{\rm ts}$ is maximized when the ratio of creep (retardation) time ($=\frac{E_0}{E_{\infty}}\tau$) to contact time $\sim 0.05-0.5$. Thus,

if a polymer surface were to have many relaxation modes, those whose relaxation and creep times are $\approx\!0.01-0.1$ and $\approx\!0.05-0.5$ of the contact time, respectively, are likely to contribute most to the energy dissipation. In this sense, the energy dissipated in AM-AFM on a viscoelastic sample may be considered as a "narrow band filter" for capturing the effect of a narrow range of polymer relaxation times.

Figure 10 illustrates $V_{\rm ts}$ and $E_{\rm ts}$ vs τ for four selected set point ratios: 0.3, 0.5, 0.7, and 0.9. These are extracted from the same

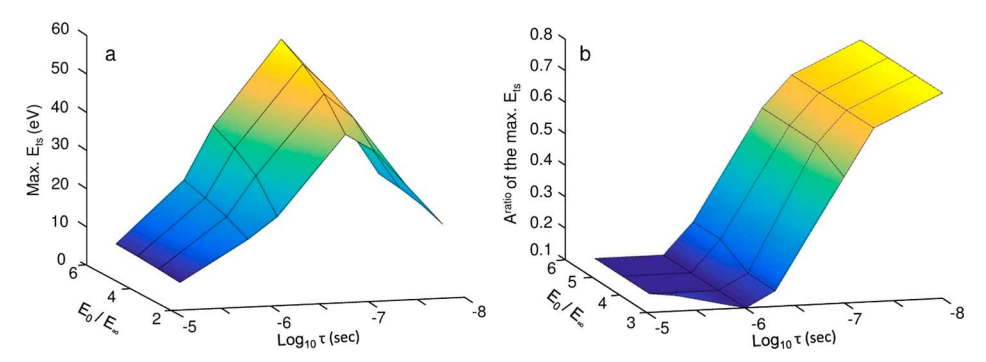


Figure 13. Maximum $E_{\rm tS}$ and $A^{\rm ratio}$ at which the maximum $E_{\rm tS}$ occurs plotted as a function of the relaxation time (τ) and E_0/E_{∞} ratio for PP. The employed material properties are listed in Table 2, $A^{\rm free}=18$ nm, K=28 N/m, and other parameters are identical to the ones described in the Experiments section.

set of simulations as in Figure 8 and are shown by vertical dashed lines marked by Roman numerals. The results show that while $E_{\rm ts}$ varies more significantly than $V_{\rm ts}$ with τ , $E_{\rm ts}$ is maximized and $V_{\rm ts}$ is minimized when the creep time is \approx 0.05–0.5 of the contact time.

The surface pressure parameters (H, z_0) that define the resultant surface adhesion, are also expected to play a role in the observed energy dissipation and hysteresis. To assess the sensitivity of $E_{\rm ts}$ vs $A^{\rm ratio}$ to these parameters, a range of H values between 2×10^{-19} and 10×10^{-19} J and a range of z_0 values between 0.5 and 0.8 nm are used in the model. For smaller values of z_0 chosen in this range, surface instabilities are observed with increased hysteresis. However, those simulations are also associated with computational instabilities. The range of z_0 chosen in these simulations is both comparable to prior computational results and appropriate for small roughness polymer surfaces. As shown in Figure 11, within the range of chosen surface pressure parameters, $E_{\rm ts}$ increases as H is increased or as z_0 is decreased. This result is in line with the expectation that energy dissipation should increase with an increase in surface forces.

2.4. Experiments. To demonstrate how the proposed computational approach relates to experimental data acquired on polymers, a set of experiments using tapping mode (TM) or AM-AFM at 326.1 kHz and quasi-static (QS) at 1 Hz are conducted on the surface of a three-component polymer blend sample. The sample consists of a glassy polymer, polycarbonate; a semicrystalline polymer, polypropylene; and a polyolefinbased elastomer. The full description of the employed instruments and sample preparation is provided in the Experimental Methods section. Typical sample data are shown in Figure 12 that are acquired over a rectangular region with the TM microcantilever with $A^{\text{free}} = 35.9 \text{ nm}$ and $A^{\text{ratio}} = 0.7$. The resulting topography image (Figure 12a) shows areas of smooth PC are interspersed with areas of PP with more surface roughness. Smaller areas of elastomer are found embedded in and surrounded by PC and PP domains. The acquired phase data are converted to phase lag ϕ and adjusted so that when drive frequency equals the microcantilever's natural frequency far from the sample then $\phi = 90^{\circ}$. For these operating conditions, the AFM mostly operates in the net repulsive regime $(\phi < 90^{\circ})$, throughout the scan region) as seen in Figure 12b. The E_{ts} values (eV per tap) are extracted from the phase lag images by using the relation³

$$E_{\rm ts}(Z, A) = \frac{\pi k A A_0}{Q} (\sin(\phi) - A^{\rm ratio})$$
(20)

and mapped to the scan region as shown in Figure 12c. Histograms of $E_{\rm ts}$ and ϕ acquired over rectangular regions of the PP, PC, and elastomer phases are shown respectively in Figures 12d and 12e.

The experimental validation of our computational approach is challenging due to uncertainties associated with the model parameters. For example, viscoelastic bulk properties can be measured using dynamic mechanical analysis (DMA). However, their correlation with viscoelastic surface properties measured using AFM methods remains an active topic of research. Specifically, with moderate to large net indentation, the contact resonance (CR) method based AFM studies have reported local elasticity values consistent with bulk DMA. 41,42 However, in AM-AFM in which gentler forces are used, indentations are much smaller, and the local properties may be more influenced by surface effects. 43-49 Moreover, the sample under consideration features significant interphase effects due to the mixture of small volumes of the three phases. Even if the AFM measures properties far from interphase regions on the sample surface, there can be subsurface interphases that influence surface AFM measurements. Last, but not the least, the surface force parameters z_0 and H are very hard to estimate experimentally. While H can be approximated using theory, there is no clearly accepted method to approximate z_0 for the specific sample.

We chose to adopt the following strategy for estimating parameters for subsequent experimental validation:

- 1. We estimate the Hamaker constants between native Si oxide on the tip surface and the specific polymer using Lifshitz theory. 40 z_0 is chosen within the range of prior works 40 and is made as small as possible to enable stable computation.
- 2. We use the QS force curves acquired on each of the three phases to estimate the long-time scale elastic modulus E_{∞} using Hertz contact mechanics. This is a reasonable approach since the QS curves are performed at extremely slow rates (1 Hz), and the quantification of uncertainties in measuring surface elastic modulus using standard force—distance curves is well understood. So
- 3. We then estimate E_0 and τ by fitting these numbers to match various features of the $E_{\rm ts}$ vs $A^{\rm ratio}$ curve acquired on the three polymer phases with $A^{\rm free} = 35.9$ nm. Specifically, for each of the polymer domains:
- a. τ is adjusted until the $A^{\rm ratio}$ at which maximum energy dissipation occurs in simulations results matches within 10% the one found in experiment. This is based on a key theoretical prediction that the $A^{\rm ratio}$ at which the maximum $E_{\rm ts}$ energy dissipation occurs is mostly affected

Macromolecules

Table 2. Material Property Estimations/Extracted from the Set of Experiments with $A^{\text{free}} = 35.9 \text{ nm}$ and Used for Subsequent Validation with a Another Set of Experiments with $A^{\text{free}} = 18 \text{ nm}$ on the Three-Polymer Blend Sample

	τ (s)	E_0 (GPa)	E_{∞} (GPa)	Н (Ј)	z_0 (nm)
elastomer	1.05×10^{-8}	2.5	0.115	8×10^{-20}	0.26
polypropylene	2.18×10^{-8}	9.01	1.64	7.6×10^{-20}	0.19
polycarbonate	4.5×10^{-9}	110	3.7	8.8×10^{-20}	0.19

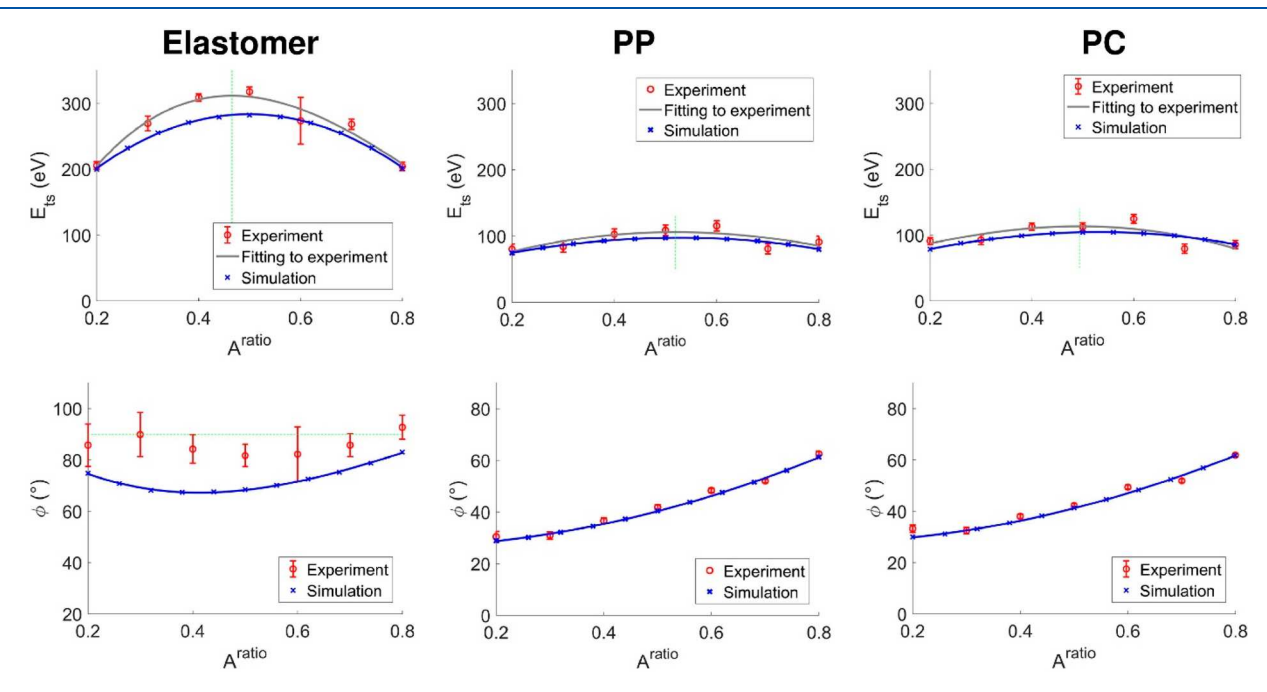


Figure 14. Comparison between theory and experiment for the three phases following calibration of τ and E_0 to best match the amount $E_{\rm ts}$ and the $A^{\rm ratio}$ at which it occurs in the experimental data acquired with $A^{\rm free}=35.9$ nm. A cubic polynomial is fitted to theory and experimental data to facilitate identification of the maximum $E_{\rm ts}$ location and magnitude. To help to clarify the regime of the oscillation, the 90° phase lag is marked by a green horizontal dashed line.

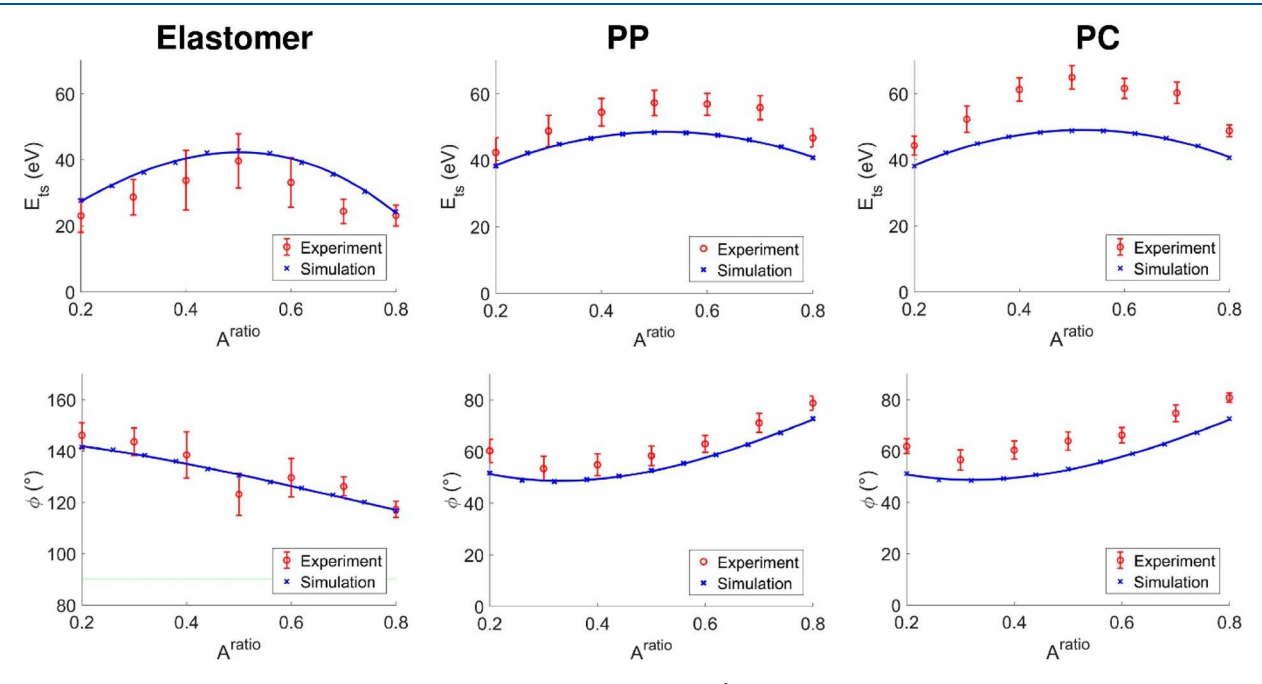


Figure 15. Comparison of computational predictions and experimental results for $A^{\text{free}} = 18$ nm on the three polymer phases. The material property data used for the computation (Table 2) are based on quasi-static force curves, theoretical estimates, and with τ and E_0 calibrated from similar data acquired for $A^{\text{free}} = 35.9$ nm (Figure 14). The observed discrepancy between simulation and experimental results is less than 11%, 11%, and 22% for elastomer, PP, and PC, respectively.

by τ (Figure 13b) and to a much lesser extent by E_0/E_∞ . As an initial starting guess τ is chosen to be 1% of the cantilever oscillation period.

- b. E_0 value is increased from E_∞ so that the maximum energy dissipation $(E_{\rm ts})$ of the model matches within 10% of the peak value of the fitted curve.
- c. τ is again tuned to ensure that the $A^{\rm ratio}$ at which maximum energy dissipation occurs in simulations remains within 10% the one in experiment.

The estimated values for the material properties using this approach are provided in Table 2. The resulting computational and experimental $E_{\rm ts}$ vs $A^{\rm ratio}$ are compared in Figure 14. As can be seen, the computational results using material properties estimated with the experimental data set at $A^{\rm free}=35.9$ nm match the experimental results within 5% across a wide range of $A^{\rm ratio}$. These estimated material properties are in line with the results provided by others. 51,52

Using the material properties estimated using the calibration data (Table 2), we validate the computational approach by comparing predictions with experimental data for $A^{\rm free}=18.0$ nm. As illustrated in Figure 15, the predicted and measured $E_{\rm ts}$ are within 10% over a wide range of $A^{\rm ratio}$ for both PP and elastomer. The good match obtained on the elastomer is particularly interesting since for $A^{\rm free}=18.0$ nm most of the approach curve is in the attractive regime of oscillation.

However, the computational approach underpredicts actual energy dissipation by over 20% for PC. In contrast with the other polymer phases in the blend, PC is hydrophilic, so that under the ambient conditions of the experiment water bridges may form leading to capillary forces and significant additional energy dissipation that are unaccounted for in the present approach. 53-55 To estimate the influence of capillary forces on the total observed energy dissipation, a set of peak force tapping experiments were conducted under ambient and dry nitrogen flushed conditions. Based on the observed results, the hysteresis of a single force cycle at ambient condition is about 8%, 7%, and 50% higher for PP, elastomer, and PC, respectively, under ambient conditions compared to under dry nitrogen. Thus, capillary forces are likely to contribute more to AM-AFM under ambient conditions on PC than on PP or elastomer and might have resulted into unrealistic predictions for PC.

Finally, it is worth mentioning that there is a potential bistability between attractive and repulsive regimes of oscillation in AM-AFM. ^{10,56,57} Under the free oscillation amplitudes considered in these simulations, the tip either remained exclusively in the attractive (for example, on the elastomer in Figure 15) or repulsive regime of oscillation in the range of set point amplitudes considered. If there is an initial attractive regime, the algorithm tracks that solution until that solution bifurcates and the algorithm jumps to the repulsive regime as the set point is decreased.

3. CONCLUSIONS

Understanding dAFM on polymers needs computational approaches in which the relevant physics of the interactions are taken into account in a self-consistent manner. By accelerating Attard's model computations and embedding it within dAFM amplitude reduction formulas it is possible to efficiently compute key dAFM observables such as surface deformation history, indentations, energy dissipation, phase, and so on as a function of the amplitude ratio. This allows the inclusion of arbitrary surface forces and linear 3D viscoelasticity

in a self-consistent manner in such simulations, representing a significant advance in computational AFM on polymers. This method alleviates the issues with the artifacts arising from the use of ad hoc viscoelastic contact mechanics models. The code and algorithm have been validated against prior results and other reliable codes. Experimental data on energy dissipation in TM-AFM/AM-AFM for different free amplitudes and amplitude ratios are presented on a three-polymer blend consisting of welldispersed phases of polypropylene, polycarbonate, and elastomer. An approach to experimental validation of computational results is presented using TM-AFM data on a blend of PP-elastomer-PC. The computational and experimental approaches presented in this work clarify the role of surface forces and polymer relaxation times on the phase lag, energy dissipation, and surface deformation history. Such approaches are expected to aid ongoing efforts to interpret dAFM observables on polymers in terms of quantitative physical properties.

4. EXPERIMENTAL METHODS

Instrument. All TM/AMAFM and QS measurements were made on a Bruker MultiMode 8 AFM with a Nanoscope V controller running v8.15 Nanoscope software. For the TM measurements, a Bruker TESF silicon microcantilever was used with a quality factor, spring constant, and fundamental frequency of 542, 28.0 N/m, and 326.1 kHz, respectively. These values were measured using thermal tuning of the undriven microcantilever. TM-AFM/AM-AFM experiments are performed on a $10 \times 5 \mu m^2$ rectangular region with 512 points/line resolution level and a scan rate of 0.5 Hz using two different free amplitudes (18.0 and 35.9 nm) and nine different amplitude ratios (0.9, 0.8, ..., 0.1). For the TM imaging, the phase was zeroed when the microcantilever was within 100 nm of the surface for each amplitude ratio measurement. QS force curves are acquired over the same sample at 200 points (5 rows \times 40 columns evenly spaced) on the same region using a Bruker TESP silicon type microcantilever whose spring constant was 21.2 N/m. By use of a blind reconstruction method, the tip radius of the QS microcantilever was estimated to be 14.2 nm and tip radius of TM microcantilever was determined to be 14.0 nm.

Sample Preparation. The sample consists of a glassy polymer, polycarbonate (Calibre 302-6, Trinseo); a semicrystalline polymer, polypropylene (Inspire 404, Braskem); and a polyolefin-based elastomer (Engage 8003, The Dow Chemical Company). The sample was fabricated using injection-compression molding providing 2 in. \times 2 in. \times 1/8 in. plaques. Pieces of the plaque were removed via a punch and mounted into vice holders. Trapezoid faces were cryo-milled in the plaques pieces at $-120~^{\circ}\text{C}$ and then polished in a cryo-microtome at $-120~^{\circ}\text{C}$ to produce block faces for AFM investigation.

ASSOCIATED CONTENT

S Supporting Information

The Supporting Information is available free of charge on the ACS Publications website at DOI: 10.1021/acs.macromol.8b01485.

Description of Video S1 (PDF)

Video S1: interaction between a rigid axisymmetric tip and the elastomer sample surface (AVI)

AUTHOR INFORMATION

Corresponding Author

*E-mail: raman@purdue.edu.

ORCID

Bahram Rajabifar: 0000-0002-4866-8339 Arvind Raman: 0000-0001-6297-5581

Notes

The authors declare no competing financial interest.

ACKNOWLEDGMENTS

The authors thank Mary Ann Jones for the molding of the three-component polymer blend and Carl Reinhardt for the cryomicrotomy of the blend. Both are from The Dow Chemical Company. Financial support for this research provided by the Dow Chemical Company and the National Science foundation through Grant CMMI-1726274 GOALI is gratefully acknowledged.

REFERENCES

- (1) Magonov, S. N.; Reneker, D. H. Characterization of polymer surfaces with atomic force microscopy. *Annu. Rev. Mater. Sci.* **1997**, 27 (1), 175–222.
- (2) Liu, Y.; Zhao, J.; Li, Z.; Mu, C.; Ma, W.; Hu, H.; Jiang, K.; Lin, H.; Ade, H.; Yan, H. Aggregation and morphology control enables multiple cases of high-efficiency polymer solar cells. *Nat. Commun.* **2014**, *5*, 5293.
- (3) Wang, D.; Nakajima, K.; Fujinami, S.; Shibasaki, Y.; Wang, J.-Q.; Nishi, T. Characterization of morphology and mechanical properties of block copolymers using atomic force microscopy: Effects of processing conditions. *Polymer* **2012**, *53* (9), 1960–1965.
- (4) Nguyen, H. K.; Fujinami, S.; Nakajima, K. Elastic modulus of ultrathin polymer films characterized by atomic force microscopy: The role of probe radius. *Polymer* **2016**, *87*, 114–122.
- (5) Nizamoglu, S.; Gather, M. C.; Humar, M.; Choi, M.; Kim, S.; Kim, K. S.; Hahn, S. K.; Scarcelli, G.; Randolph, M.; Redmond, R. W.; Yun, S. H. Bioabsorbable polymer optical waveguides for deep-tissue photomedicine. *Nat. Commun.* **2016**, *7*, 10374.
- (6) Calleja, M.; Nordström, M.; Álvarez, M.; Tamayo, J.; Lechuga, L. M.; Boisen, A. Highly sensitive polymer-based cantilever-sensors for DNA detection. *Ultramicroscopy* **2005**, *105* (1), 215–222.
- (7) Raghavan, D.; Gu, X.; Nguyen, T.; VanLandingham, M.; Karim, A. Mapping polymer heterogeneity using atomic force microscopy phase imaging and nanoscale indentation. *Macromolecules* **2000**, 33 (7), 2573–2583.
- (8) Tamayo, J.; Garcia, R. Deformation, contact time, and phase contrast in tapping mode scanning force microscopy. *Langmuir* **1996**, 12 (18), 4430–4435.
- (9) Winkler, R.; Spatz, J.; Sheiko, S.; Möller, M.; Reineker, P.; Marti, O. Imaging material properties by resonant tapping-force microscopy: a model investigation. *Phys. Rev. B: Condens. Matter Mater. Phys.* **1996**, 54 (12), 8908.
- (10) Garcia, R.; Perez, R. Dynamic atomic force microscopy methods. *Surf. Sci. Rep.* **2002**, 47 (6), 197–301.
- (11) Cartagena-Rivera, A. X.; Wang, W.-H.; Geahlen, R. L.; Raman, A. Fast, multi-frequency, and quantitative nanomechanical mapping of live cells using the atomic force microscope. *Sci. Rep.* **2015**, *5*, 11692.
- (12) Chyasnavichyus, M.; Young, S. L.; Tsukruk, V. V. Recent advances in micromechanical characterization of polymer, biomaterial, and cell surfaces with atomic force microscopy. *Jpn. J. Appl. Phys.* **2015**, 54 (8S2), 08LA02.
- (13) Tamayo, J.; García, R. Effects of elastic and inelastic interactions on phase contrast images in tapping-mode scanning force microscopy. *Appl. Phys. Lett.* **1997**, *71* (16), 2394–2396.
- (14) Garcia, R.; Gómez, C.; Martinez, N.; Patil, S.; Dietz, C.; Magerle, R. Identification of nanoscale dissipation processes by dynamic atomic force microscopy. *Phys. Rev. Lett.* **2006**, *97* (1), 016103.
- (15) Melcher, J.; Carrasco, C.; Xu, X.; Carrascosa, J. L.; Gómez-Herrero, J.; de Pablo, P. J.; Raman, A. Origins of phase contrast in the atomic force microscope in liquids. *Proc. Natl. Acad. Sci. U. S. A.* **2009**, *106* (33), 13655–13660.
- (16) James, P.; Antognozzi, M.; Tamayo, J.; McMaster, T.; Newton, J.; Miles, M. Interpretation of contrast in tapping mode AFM and shear force microscopy. A study of nafion. *Langmuir* **2001**, *17* (2), 349–360.

(17) Cheng, D.; Yang, G.; Xi, Z. Nonlinear systems possessing linear symmetry. *International Journal of Robust and Nonlinear Control* **2007**, 17 (1), 51–81.

- (18) Melcher, J.; Hu, S.; Raman, A. Invited Article: VEDA: A webbased virtual environment for dynamic atomic force microscopy. *Rev. Sci. Instrum.* **2008**, *79* (6), 061301.
- (19) Ting, T. The contact stresses between a rigid indenter and a viscoelastic half-space. *J. Appl. Mech.* **1966**, 33 (4), 845–854.
- (20) Haviland, D. B.; van Eysden, C. A.; Forchheimer, D.; Platz, D.; Kassa, H. G.; Leclère, P. Probing viscoelastic response of soft material surfaces at the nanoscale. *Soft Matter* **2016**, *12* (2), 619–624.
- (21) Solares, S. D. A simple and efficient quasi 3-dimensional viscoelastic model and software for simulation of tapping-mode atomic force microscopy. *Beilstein J. Nanotechnol.* **2015**, 6 (1), 2233–2241.
- (22) Attard, P. Measurement and interpretation of elastic and viscoelastic properties with the atomic force microscope. *J. Phys.: Condens. Matter* **2007**, *19* (47), 473201.
- (23) Attard, P. Interaction and deformation of viscoelastic particles. 2. Adhesive particles. *Langmuir* **2001**, *17* (14), 4322–4328.
- (24) Attard, P. Interaction and deformation of viscoelastic particles: Nonadhesive particles. *Phys. Rev. E: Stat. Phys., Plasmas, Fluids, Relat. Interdiscip. Top.* **2001**, 63 (6), 061604.
- (25) Attard, P. Interaction and deformation of elastic bodies: origin of adhesion hysteresis. *J. Phys. Chem. B* **2000**, *104* (45), 10635–10641.
- (26) Attard, P.; Parker, J. L. Deformation and adhesion of elastic bodies in contact. *Phys. Rev. A: At., Mol., Opt. Phys.* **1992**, 46 (12), 7959.
- (27) Boussinesq, J. Application des potentiels à l'étude de l'équilibre et du mouvement des solides élastiques: principalement au calcul des déformations et des pressions que produisent, dans ces solides, des efforts quelconques exercées sur une petite partie de leur surface ou de leur intérieur: mémoire suivi de notes étendues sur divers points de physique, mathematique et d'analyse; Gauthier-Villars: 1885; Vol. 4.
- (28) Kiracofe, D.; Melcher, J.; Raman, A. Gaining insight into the physics of dynamic atomic force microscopy in complex environments using the VEDA simulator. *Rev. Sci. Instrum.* **2012**, 83 (1), 013702.
- (29) Anczykowski, B.; Krüger, D.; Babcock, K.; Fuchs, H. Basic properties of dynamic force spectroscopy with the scanning force microscope in experiment and simulation. *Ultramicroscopy* **1996**, *66* (3), 251–259.
- (30) Rodriguez, T. R.; García, R. Tip motion in amplitude modulation (tapping-mode) atomic-force microscopy: Comparison between continuous and point-mass models. *Appl. Phys. Lett.* **2002**, *80* (9), 1646–1648.
- (31) Raman, A.; Melcher, J.; Tung, R. Cantilever dynamics in atomic force microscopy. *Nano Today* **2008**, 3 (1), 20–27.
- (32) Garcia, R.; Gomez, C.; Martinez, N.; Patil, S.; Dietz, C.; Magerle, R. Identification of nanoscale dissipation processes by dynamic atomic force microscopy. *Phys. Rev. Lett.* **2006**, *97* (1), 016103.
- (33) Anczykowski, B.; Gotsmann, B.; Fuchs, H.; Cleveland, J.; Elings, V. How to measure energy dissipation in dynamic mode atomic force microscopy. *Appl. Sci.* **1999**, *140* (3), 376–382.
- (34) Lozano, J. R.; Garcia, R. Theory of phase spectroscopy in bimodal atomic force microscopy. *Phys. Rev. B: Condens. Matter Mater. Phys.* **2009**, 79 (1), 014110.
- (35) Melcher, J.; Hu, S.; Raman, A. Equivalent point-mass models of continuous atomic force microscope probes. *Appl. Phys. Lett.* **2007**, *91* (5), 053101.
- (36) Brinson, H. F.; Brinson, L. C. Polymer Engineering Science and Viscoelasticity; Springer: 2008.
- (37) Pethica, J.; Sutton, A. On the stability of a tip and flat at very small separations. *J. Vac. Sci. Technol., A* **1988**, *6* (4), 2490–2494.
- (38) Smith, J. R.; Bozzolo, G.; Banerjea, A.; Ferrante, J. Avalanche in adhesion. *Phys. Rev. Lett.* **1989**, *63* (12), 1269.
- (39) Martínez, N. F.; García, R. Measuring phase shifts and energy dissipation with amplitude modulation atomic force microscopy. *Nanotechnology* **2006**, *17* (7), S167.
- (40) Israelachvili, J. N. Intermolecular and Surface Forces, revised 3rd ed.; Academic Press: 2011.

(41) Hurley, D. C.; Campbell, S. E.; Killgore, J. P.; Cox, L. M.; Ding, Y. Measurement of Viscoelastic Loss Tangent with Contact Resonance Modes of Atomic Force Microscopy. *Macromolecules* **2013**, *46* (23), 9396–9402.

- (42) Yablon, D. G.; Gannepalli, A.; Proksch, R.; Killgore, J.; Hurley, D. C.; Grabowski, J.; Tsou, A. H. Quantitative Viscoelastic Mapping of Polyolefin Blends with Contact Resonance Atomic Force Microscopy. *Macromolecules* **2012**, *45* (10), 4363–4370.
- (43) Keddie, J. L.; Jones, R. A.; Cory, R. A. Size-dependent depression of the glass transition temperature in polymer films. *EPL (Europhysics Letters)* **1994**, 27 (1), 59.
- (44) Zhang, Y.-F.; Bai, S.-L.; Yang, D.-Y.; Zhang, Z.; Kao-Walter, S. Study on the viscoelastic properties of the epoxy surface by means of nanodynamic mechanical analysis. *J. Polym. Sci., Part B: Polym. Phys.* **2008**, 46 (3), 281–288.
- (45) Torres, J. M.; Stafford, C. M.; Vogt, B. D. Elastic Modulus of Amorphous Polymer Thin Films: Relationship to the Glass Transition Temperature. *ACS Nano* **2009**, *3* (9), 2677–2685.
- (46) Belikov, S.; Erina, N.; Huang, L.; Su, C.; Prater, C.; Magonov, S.; Ginzburg, V.; McIntyre, B.; Lakrout, H.; Meyers, G. Parametrization of atomic force microscopy tip shape models for quantitative nanomechanical measurements. *Journal of Vacuum Science & Technology B: Microelectronics and Nanometer Structures Processing, Measurement, and Phenomena* **2009**, 27 (2), 984–992.
- (47) Giró-Paloma, J.; Roa, J.; Díez-Pascual, A. M.; Rayón, E.; Flores, A.; Martínez, M.; Chimenos, J.; Fernández, A. Depth-sensing indentation applied to polymers: A comparison between standard methods of analysis in relation to the nature of the materials. *Eur. Polym. J.* **2013**, *49* (12), 4047–4053.
- (48) Lakrout, H.; Meyers, G. Contact mechanics of a viscoelasto-plastic film bonded to a rigid substrate. *Proc. Annu. Meet. Adhes. Soc.* **2010**, 33, 304–306.
- (49) Lakrout, H.; Valeriy, G.; Greg, M.; Bob, M.; Sergey, B.; Natalia, E.; Lin, H.; Sergei, M.; Craig, P. Quantitative AFM-based nano-indentation of poly(dimethylsiloxane) films. *Proc. Annu. Meet. Adhes. Soc.* **2008**, *31*, 392–394.
- (50) Wagner, R.; Moon, R.; Pratt, J.; Shaw, G.; Raman, A. Uncertainty quantification in nanomechanical measurements using the atomic force microscope. *Nanotechnology* **2011**, *22* (45), 455703.
- (51) Lagakos, N.; Jarzynski, J.; Cole, J.; Bucaro, J. Frequency and temperature dependence of elastic moduli of polymers. *J. Appl. Phys.* **1986**, *59* (12), 4017–4031.
- (52) Koblar, D.; Boltežar, M. Evaluation of the Frequency-Dependent Young's Modulus and Damping Factor of Rubber from Experiment and Their Implementation in a Finite-Element Analysis. *Exp. Tech.* **2016**, 40, 235.
- (53) Sahagún, E.; García-Mochales, P.; Sacha, G.; Sáenz, J. J. Energy dissipation due to capillary interactions: hydrophobicity maps in force microscopy. *Phys. Rev. Lett.* **2007**, *98* (17), 176106.
- (54) Zitzler, L.; Herminghaus, S.; Mugele, F. Capillary forces in tapping mode atomic force microscopy. *Phys. Rev. B: Condens. Matter Mater. Phys.* **2002**, *66* (15), 155436.
- (55) Cleveland, J.; Anczykowski, B.; Schmid, A.; Elings, V. Energy dissipation in tapping-mode atomic force microscopy. *Appl. Phys. Lett.* **1998**, 72 (20), 2613–2615.
- (56) Lee, S.; Howell, S.; Raman, A.; Reifenberger, R. Nonlinear dynamic perspectives on dynamic force microscopy. *Ultramicroscopy* **2003**, *97* (1–4), 185–198.
- (57) Garcia, R.; San Paulo, A. Dynamics of a vibrating tip near or in intermittent contact with a surface. *Phys. Rev. B: Condens. Matter Mater. Phys.* **2000**, *61* (20), R13381.